RESEARCH ARTICLE

Yian LU, Suxin QIAN, Jun SHEN

A fully solid-state cold thermal energy storage device for car seats using shape-memory alloys

Abstract Thermal energy storage has been a pivotal technology to fill the gap between energy demands and energy supplies. As a solid-solid phase change material, shape-memory alloys (SMAs) have the inherent advantages of leakage free, no encapsulation, negligible volume variation, as well as superior energy storage properties such as high thermal conductivity (compared with ice and paraffin) and volumetric energy density, making them excellent thermal energy storage materials. Considering these characteristics, the design of the shape-memory alloy based the cold thermal energy storage system for precooling car seat application is introduced in this paper based on the proposed shape-memory alloy-based cold thermal energy storage cycle. The simulation results show that the minimum temperature of the metal boss under the seat reaches 26.2 °C at 9.85 s, which is reduced by 9.8 °C, and the energy storage efficiency of the device is 66%. The influence of initial temperature, elastocaloric materials, and the shape-memory alloy geometry scheme on the performance of car seat cold thermal energy storage devices is also discussed. Since SMAs are both solid-state refrigerants and thermal energy storage materials, hopefully the proposed concept can promote the development of more promising shape-memory alloy-based cold and hot thermal energy storage devices.

1 Introduction

Technological advancement and economic development rely on energy for society to progress. The depletion of non-renewable fossil fuels and the escalating global warming crisis call for developing sustainable and renewable energy sources [1, 2]. Considering the unstable and discontinuous nature of renewable energy sources such as solar energy, thermal energy storage (TES) has been a pivotal technology to fill the gap between energy demand and renewable energy sources [3, 4], which has a great application potential in the future. Phase change materials offer a promising high-energy density solution to store cold thermal energy. Compared with solid-liquid phase change materials, such as paraffin or ice, solid-solid phase change materials have the inherent advantages of leakage free, no encapsulation, and negligible volumetric variation [5–7]. Shape-memory alloys (SMAs), which are typical solid-solid phase change materials, also have merits of high thermal conductivity (compared with ice and paraffin), colossal volumetric energy density, and superior discharge rate [8, 9], making them excellent thermal energy storage materials.

The elastocaloric effect (eCE) in SMAs is a phenomenon in entropy and temperature change when mechanical stress is applied or released. During the mechanical loading and unloading process, the strain experiences a significant change, indicating a first-order phase transition [10], and such nominally reversible loading and unloading characteristics have been known as the superelastic effect. A refrigerator based on this principle has been recently reported [11]. Most importantly, the principle of shape-memory phase transfor-

Yian LU
Department of Refrigeration and Cryogenic Engineering, Xi'an Jiaotong University, Xi'an 710049, China; Key Laboratory of Cryogenics, Technical Institute of Physics and Chemistry, Chinese Academy of Sciences, Beijing 100190, China

Suxin QIAN (✉)
Department of Refrigeration and Cryogenic Engineering, Xi'an Jiaotong University, Xi'an 710049, China
E-mail: qiansuxin@xjtu.edu.cn

Jun SHEN
Key Laboratory of Cryogenics, Technical Institute of Physics and Chemistry, Chinese Academy of Sciences, Beijing 100190, China; Department of Energy and Power Engineering, School of Mechanical Engineering, Beijing Institute of Technology, Beijing 100081, China

mation as a class of metallic solid-solid phase change materials has been proposed by the US Army Research Laboratory [8]. NiTiHf, an SMA thermal energy storage material, features an energy density of 260 MJ/m³, which is comparable to some of the typical liquid-solid phase change materials such as paraffin and hydrated salts, but with much higher thermal conductivity at more than 10 W/(m·K) [12]. A water-based SMA thermal energy storage device using commercial NiTi has been constructed and tested by the same research group, where a 1.7 – 3.3 improvement in volumetric energy density was experimentally achieved when compared with the baseline sensible energy storage device [13]. However, these efforts have been made only to investigate the storage of thermal energy by leveraging the stress-free heat driven phase transition. Thus, more efforts have to be made toward the storage of cold thermal energy using stress-induced phase transition or a combination of heat driven phase transition and stress-induced phase transition.

Although SMAs have been identified and demonstrated as ultra-high performance metalic solid-solid phase change materials for cyclic energy storage [8, 13], most studies have been focusing on the energy storage properties of SMAs [9, 14–16]. Although these studies demonstrate the feasibility of SMA-based energy storage, it is still not clear how to design and construct a TES device based on this concept. On the other hand, there are a few developed elastocaloric cooling and heat pump prototypes [17–20] that are continuously operated. The ingredients in the elastocaloric cooling systems can inspire the SMA-based TES devices, yet additional efforts are needed to complement their unique discontinuous operation characteristics.

Aiming to fill the gap in cold thermal energy storage using SMA, this paper first introduced the concept of cold thermal energy storage using SMA. Then, based on eCE, in the design of the cold thermal energy storage device, and the theoretical analysis of the device, it considered the high thermal conductivity of SMAs and the challenge of designing a heat transfer surface suitable for both discharging the stored cold thermal energy and the release of heat during the charging process. Next, considering these characteristics, it introduced the design philosophy of the SMA-based cold thermal energy storage system for car seat application. Finally, it discussed in detail the energy discharge characteristics of the SMA cold thermal energy storage device based on a transient simulation model. This study will be a first step toward developing real SMA-based cold thermal energy storage devices.

2   Theoretical cycle of SMA-based cold thermal energy storage

At ambient temperatures, such as in this paper, the SMA should be initially fully austenite. That means that the transformation temperature (T_{A_r}) should be lower than the minimum operating temperature of the overall system, essentially the premise of the stress-induced phase transformation process [21].

According to Fig. 1, phase transition occurs when the stress on SMA exceeds the critical stress of phase transition (σ^{AM}). Upon loading, the SMA changes from the parent phase austenite to the high-pressure martensite phase, and after that, it is stored at ambient temperature. Meanwhile, the latent heat is first transformed into internal energy and then released to the ambient. A radiator is usually required to assist with the dissipation of latent heat. After releasing the latent heat, the SMA is fully charged and is 'frozen' in the high-pressure martensite phase until the discharging process. The 'frozen' state is held on until triggered by the control command for discharging.

The load is instantly removed when cooling capacity is needed, which is the abovementioned triggering signal. Once the applied stress decreases below the critical stress (σ^{MA}), the reverse phase transition from martensite to austenite takes place, which causes the entropy of SMA to increase, thereby permitting it to absorb the heat from the cooling target.

Compared with the continuous elastocaloric cooling cycle in a refrigerator [11], the cold thermal energy storage cycle is discontinuous and operates on demand. Figure 1 shows the theoretical cycle of cold thermal energy storage. The two processes, i.e., the charging process and the discharging process, include six stages with shape and color variations to differentiate phase states and temperature states, respectively. The charging and discharging processes are triggered upon receiving the control signal, which varies in different applications.

The cold thermal energy storage cycle is plotted in the temperature-stress diagram and temperature-entropy diagram in Fig. 2, in which the red line and blue line respectively represent the charging process and the discharging process, which is the same as those in Fig. 1. The numbers in Fig. 2 also correspond to the same state of SMA as those in Fig. 1. The red shaded area in Fig. 2 represents the boundary of all possible charging processes.

2.1   Charging process

When loading the stress-free SMA, the stress increases at isothermal temperature since the martensitic transformation has not yet occurred, which corresponds to states 1 to 2 in Fig. 2. Upon exceeding the minimum stress (σ^{AM}) required to undergo martensitic transformation at the temperature of state 2, the SMA begins to transform from the parent austenite phase to the high-pressure martensite phase, as shown in states 2 to 3 in Fig. 2. The temperature of SMA increases with increasing stress after that. By reaching state 3, the temperature of SMA reaches the maximum among the cold thermal energy storage cycles. The slope of 2−3 depends on the loading and
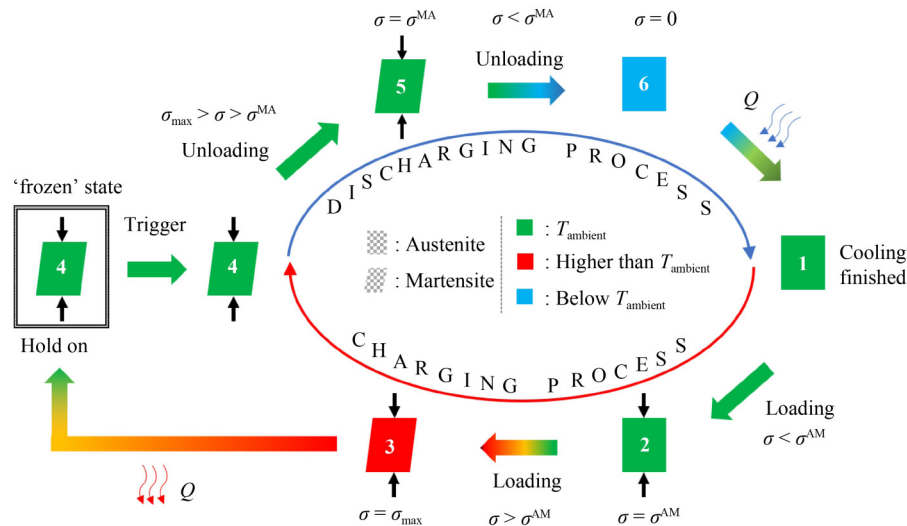
Fig. 1   Theoretical cycle of SMA-based cold thermal energy storage.
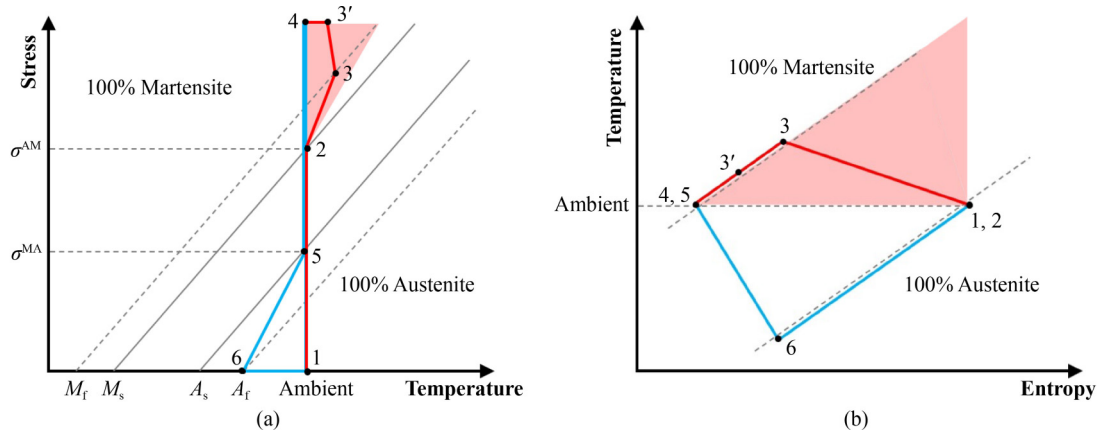

Fig. 2   SMA cold thermal energy storage cycle.
(a) Stress−temperature diagram; (b) temperature−entropy diagram.

charging rate, where infinitely slow loading may result in isothermal loading while infinitely fast loading leads to isentropic loading, which dictates the boundary of the red-shaded area in Fig. 2. Generally, at state 3, the SMA will be further compressed to 3′ to ensure being fully martensite. Meanwhile, the SMA, whose temperature is higher than the ambient temperature, dissipates heat to the environment until it is in equilibrium with the ambient temperature, as can be observed in Fig. 2 (3-3′-4). This process can be maintained for any time until a discharging signal triggers the discharging process, which is the most significant difference between the proposed SMA-based cold thermal energy storage cycle and the conventional eC cooling cycle (the difference in the time scale is not shown in Fig. 2).

2.2   Discharging process

In the unloading process, the SMA maintains a 100%

martensitic phase at first until the stress on it is reduced below the critical stress (σ^{MA}). After that, the phase transformation from the high-pressure martensite phase to the parent austenite phase starts, which corresponds to states 5 to 6 in Fig. 2. The SMA reaches its lowest temperature at state 6 when it has completed the reverse transformation, which also indicates that the SMA transforms into the austenite phase entirely. The SMA then absorbs the heat from the cooling target, corresponding to the endothermic process 6 to 1 in Fig. 2. Through this process (6 to 1), the cooling from SMA is transferred to the cooling target.

3   Mechanical design of car seat cold thermal energy storage device

Now consider applying the SMA cold thermal energy storage cycle to precool the car seats. On a sunny day, the

cabinet temperature and seat temperature may exceed far beyond ambient temperature, and at least a few minutes of ventilation and air conditioning are needed to cool the car seats. When detecting the entrance of the driver and the passengers, the SMA-based cold thermal energy storage device can discharge the stored cold thermal energy and instantly cool car seats before the air conditioning system starts, thus improving the thermal comfort for the driver and passengers. The SMA cold thermal energy storage system only needs to cool the car seat once and the vehicle air conditioning system will handle the cooling for the rest of the trip. The SMA will be charged again once the driver and passengers leave the vehicle after the trip ends.

The car seat cold thermal energy storage device is installed under the car seat. Figure 3(a) illustrates how the SMA is loaded and unloaded using the shape characteristics of the V-pattern slide track (1), and the motor is controlled by the seat pressure sensor (4) to indicate if seat cooling is needed. The strain of the SMA changes when it moves up and down in the V-shaped slide track (1), which causes martensitic transformation upon loading and reverse transformation when stress is released. The motor and pulley (3) are fixed on the bottom of the frame. As this motor starts, the steel cable (5) can be tensioned; as it stops, the restraint on the steel cable (5) disappears, allowing it to be freely extended.

At one end, as the driving medium, the SMA clamp (2) is connected to the motor shaft, while the other is connected to the steel cable (5). Constrained by the pulling action of the steel cable (5) and the inclined slide track (1), the SMA is compressed as it moves downward, thus driving it to undergo martensitic phase transformation.

As demonstrated in Fig. 3(b), the SMA is in contact with the heat sink in the compressed state when it releases latent heat. When the SMA is unloaded, it absorbs heat when it is in contact with the metal boss under the seat to cool the seat, as displayed in Fig. 3(c). A pressure sensor (4) on the seat controls the start and stop of the motor; if the sensor detects no pressure, i.e., when no one is seated in the seat, the motor runs to store the cold thermal energy; if it detects pressure, i.e., when the driver or passenger sits in the seat, the motor stops and the stored cold thermal energy is released.

A set of linear bearings can make the slide track (1) slider stay in the horizontal plane by adding pressure uniaxially, as depicted in Fig. 3(d). A clamp that prevents SMA from bending and buckling is used to hold it in the middle of the horizontal slideway, as illustrated in Fig. 3(e). The anti-buckling clamp has a more extended lower clip, the middle of which is connected to a spring, making it convenient to fold and unfold during loading and unloading. As a result of the presence of the lower clip, the freedom in the lateral direction can be decreased, and the buckling deformation of the SMA can be significantly reduced.

4   Simulation model

The core of the cold thermal energy storage system is the SMA with eCE. Based on the energy equation applied in Ref. [22], this paper adopts its variation in the two-dimensional form. In Eq. (1), the left-hand term represents transient energy storage, while the right-hand terms correspond to diffusion and eCE, respectively.
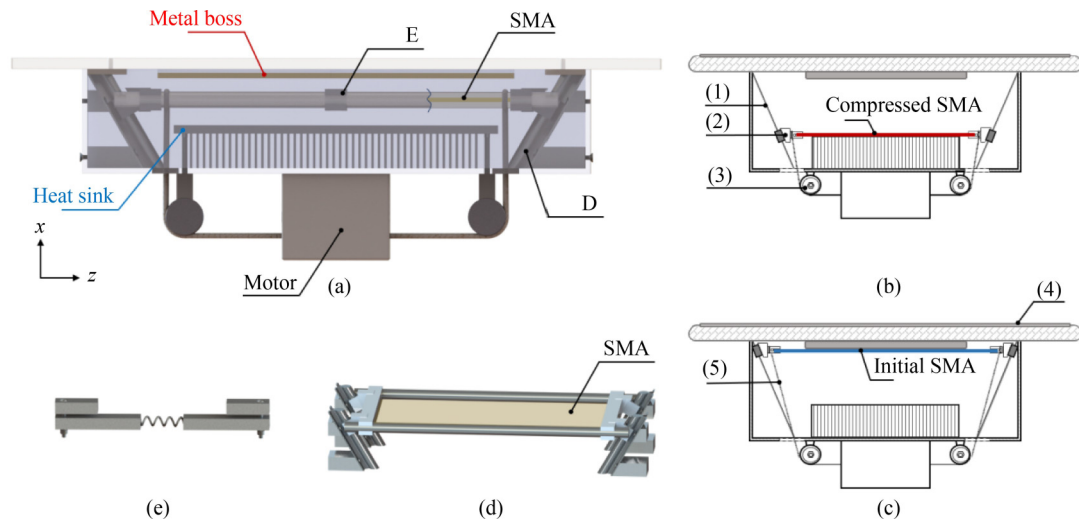

Fig. 3   Illustration of the car seat cold thermal energy storage device ((1) slide track, (2) clamp, (3) pulley, (4) pressure sensor, and (5) steel cable).

(a) Overall appearance; (b) final status of the charging process: releasing heat to the ambient via the heat sink; (c) final status of the discharging process: cooling the metal boss under the seat; (d) horizontal and vertical slides; (e) anti-buckling clamp.

$$(\rho c)_{\mathrm{m}}\frac{\partial T_{\mathrm{m}}}{\partial t} = \left[\frac{\partial}{\partial x}\left(k(\xi)\frac{\partial T_{\mathrm{m}}}{\partial x}\right) + \frac{\partial}{\partial y}\left(k(\xi)\frac{\partial T_{\mathrm{m}}}{\partial y}\right)\right] + g''', \quad (1)$$

where the subscript $_{\mathrm{m}}$ represents the SMA, and due to the large difference between the austenite phase and martensite phase, $k(\xi)$ denotes a phase-dependent thermal conductivity, which is calculated locally based on k_{A} and k_{M} as

$$k(\xi) = \left(\frac{\xi_{\mathrm{M}}}{k_{\mathrm{M}}} + \frac{\xi_{\mathrm{A}}}{k_{\mathrm{A}}}\right)^{-1}. \quad (2)$$

The energy equation of the metal boss under the seat is

$$\frac{\partial T_{\kappa}}{\partial t} = a_{\kappa}\left(\frac{\partial^2 T_{\kappa}}{\partial x^2} + \frac{\partial^2 T_{\kappa}}{\partial y^2}\right). \quad (3)$$

Equation (1) emphasizes the importance of the eCE, which is determined by the martensitic phase transformation rate as expressed in Eq. (4) [23].

$$g''' = \rho_{\mathrm{m}} T_{\mathrm{m}} \Delta s \cdot \dot{\xi}_{\mathrm{M}}. \quad (4)$$

In the MAS-PF model developed by Wendler et al. [24], the coexisting phases are austenite A, tension martensite phase M_+, and compression martensite phase M_-. This paper does not distinguish between the densities of austenite and martensite, which are collectively referred to as phase fractions since they have the same density and the mass-based phase fraction is numerically equal to the volume-based phase fraction. Since the compressive pseudoelastic characteristics of elastocaloric cooling is focused on, where only the compressed martensite and austenite coexist, the compressed martensite phase fraction (ξ_{M_-}) is abbreviated as ξ_{M}. Based on the transition kinetic model, rate equations for the phase fractions of austenite (ξ_{A}) and compression martensite (ξ_{M}) are formulated as

$$\dot{\xi}_{\mathrm{M}} = -\xi_{\mathrm{M}} \cdot p^{\mathrm{MA}}(T_{\mathrm{m}},\sigma) + \xi_{\mathrm{A}} \cdot p^{\mathrm{AM}}(T_{\mathrm{m}},\sigma), \quad (5)$$

where the conservation constraint applies to both the austenite phase fraction and the martensitic phase fraction,

$$\xi_{\mathrm{M}} + \xi_{\mathrm{A}} = 1. \quad (6)$$

The approximation formula for phase transition rate $p^{\alpha\beta} (\alpha, \beta = \mathrm{A}, \mathrm{M})$ is applied as

$$p^{\mathrm{MA}}(T_{\mathrm{m}},\sigma) =$$
$$\begin{cases} \frac{1}{\tau}\sqrt{\frac{E_{\mathrm{M}}}{E_{\mathrm{A}}}}\mathrm{erfc}\left[-0.910\sqrt{\frac{V_{\mathrm{L}}}{2E_{\mathrm{M}}k_{\mathrm{B}}T}}(\sigma^{\mathrm{MA}} - \sigma)\right], & \sigma > \sigma^{\mathrm{MA}}, \\ \frac{1}{\tau}\sqrt{\frac{E_{\mathrm{M}}}{E_{\mathrm{A}}}}, & \sigma \leqslant \sigma^{\mathrm{MA}}, \end{cases}$$
$$(7)$$

$$p^{\mathrm{AM}}(T_{\mathrm{m}},\sigma) =$$
$$\begin{cases} \frac{1}{\tau}\mathrm{erfc}\left[0.910\sqrt{\frac{V_{\mathrm{L}}}{2E_{\mathrm{M}}k_{\mathrm{B}}T}}(\sigma^{\mathrm{AM}} - \sigma)\right], & \sigma < \sigma^{\mathrm{AM}}, \\ \frac{1}{\tau}, & \sigma \geqslant \sigma^{\mathrm{AM}}. \end{cases}$$
$$(8)$$

Equations (9) and (10), which show the most widely adopted linear correlation, can be used to determine the transformation stress.

$$\sigma^{\mathrm{AM}}(T_{\mathrm{m}}) = C_{\mathrm{AM}}(T_{\mathrm{m}} - T_{\mathrm{Ms}}), \quad (9)$$

$$\sigma^{\mathrm{MA}}(T_{\mathrm{m}}) = C_{\mathrm{MA}}(T_{\mathrm{m}} - T_{\mathrm{As}}). \quad (10)$$

The linear constitutive relation between stress and strain is adopted, as expressed in Eq. (11).

$$\varepsilon(\sigma, T_{\mathrm{m}}, \xi_{\mathrm{M}}) = \xi_{\mathrm{A}}\frac{\sigma}{E_{\mathrm{A}}} + \xi_{\mathrm{M}}\left(\varepsilon_{\mathrm{T}} + \frac{\sigma}{E_{\mathrm{M}}}\right). \quad (11)$$

The unloading control strategy is to control the SMA deformation during the unloading process, which determines the transformation evolution of the SMA. Under the premise of simplification and without loss of generality, this part adopts a linear model for the strain variation model of SMA in the unloading process.

$$\dot{\varepsilon} = \mathrm{const}, \quad (12)$$

$$\varepsilon|_{t=0} = \varepsilon_{\max}. \quad (13)$$

All equations mentioned are coupled together, including the energy equations, the transformation kinetic equations, the constitutive equation, the unloading control equations, and the energy equation of the metal boss. These couplings can be seen in Fig. 4. The evolution of the martensite component of the SMA and the temperature change of both the metal boss and the SMA can be simultaneously solved.
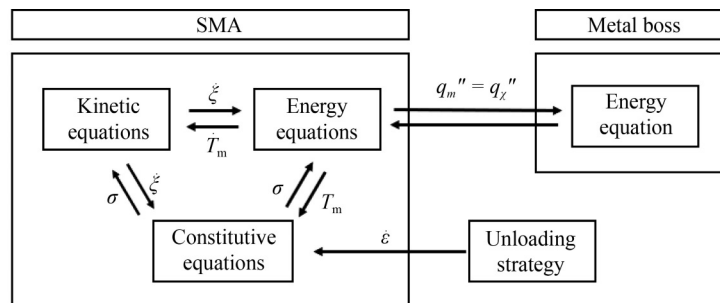

Fig. 4 Block diagrams of simulation model.

The cooling capacity of a single discharging process Q_{pro}, the cooling TES efficiency η, and the cooling COP of the TES device are used as performance evaluation criteria. Q_{pro} is defined as the latent heat storage of the SMA due to the martensitic transformation, which is calculated by Eq. (14).

$$Q_{pro} = \sum \int_0^t V_{m,i} \cdot g''' \, dt. \tag{14}$$

η is defined as the ratio of the actual discharged cooling capacity to the maximum stored cooling capacity in one cycle, which is expressed in Eq. (15).

$$\eta = \frac{Q_{use}}{Q_c} = \frac{\sum cm_i \Delta T_i}{Q_{pro} + \sum cm_{m,i}(T_{\kappa,i} - T_{m,i})}, \tag{15}$$

where the second term in the denominator is the sensible heat stored in the SMA, as manifested by the temperature difference between the SMA and the cooled object before the transformation.

COP is the ratio of the actual discharged cooling capacity to the primary power consumption of the device in each charging-discharging cycle, which is expressed in Eq. (16).

$$COP = \frac{Q_{use}}{\sum V_i \int \sigma_i d\varepsilon}, \tag{16}$$

where the power consumption is calculated by the material properties and the predicted stress-strain characteristics.

In this paper, it is assumed that the temperature of the SMA and the metal boss is uniform along the z axis. Therefore, the temperature distribution in the $x-y$ plane is discretized into n control volumes of 1×1 (mm × mm). A cold thermal energy storage cycle in the car seat cold thermal energy storage device can be divided into four stages, i.e., the slow loading stage, the stationary heat exchange stage I, the rapid unloading stage, and the stationary heat exchange stage II. The cooling eCE is only involved during the rapid unloading stage and the stationary heat exchange stage II. Table 1 presents the meshing of the numerical model and its boundary

conditions of the rapid unloading stage and the stationary heat exchange stage II, respectively. The solid-solid heat exchange between the metal boss and the SMA is modeled using a constant heat transfer coefficient in the stationary heat exchange stage II.

It is assumed in the model that there is no air between the SMA and the metal boss; the change in ambient temperature is neglected in the calculation time; only the z-direction deformation occurs in the SMA; and the segments of the SMA are treated as single-crystals with local phase fractions, and the polycrystalline characteristics are disregarded [22].

Ni-Ti alloy is selected as the SMA material while copper with a high thermal conductivity is chosen as the metal boss material. The parameters of the simulation model are listed in Table 2. With the above assumptions and formulations, this simulation model was implemented in MATLAB Simulink. The aforementioned model with the same governing equations and similar boundary conditions has been experimentally validated in Ref. [11], and the full-scale validation of the theoretical predictions will be reported in the future, once the prototype SMA-based TES device is properly functioning.
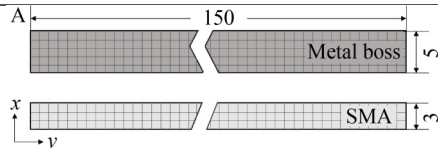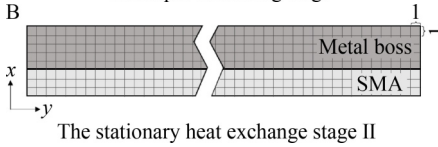
5 Results and discussion

Here, the performance during the discharging of cold thermal energy is mainly discussed. It is assumed that the cold thermal energy is fully charged.

5.1 Transient characteristics of discharging process

The temperature variation of the upper surface midpoint of the metal boss within 50 s and the breakdown of cooling capacity are plotted in Fig. 5(a). The formulas for each component in Fig. 5 are calculated by Eqs. (17)–(19). Figure 5(b) shows the transients of stress, heat exchange rate, and specific entropy. The heat exchange rate ($q_{exchange}$) refers to the amount of heat absorbed by NiTi. The specific entropy is formulated as Eq. (20)

Table 1 Introduction of meshing details and the boundary conditions

Meshing details	Boundary conditions
A $\longleftarrow$ 150 $\longrightarrow$ Metal boss — 5 — SMA — 3 — The rapid unloading stage	$k_m \left. \dfrac{\partial T_m}{\partial x} \right|_{x=0; \, x=x_{max}} = k_m \left. \dfrac{\partial T_m}{\partial y} \right|_{y=0; \, y=y_{max}} = h(T_f - T_m)$
B Metal boss — 1 — SMA The stationary heat exchange stage II	$k_\kappa \left. \dfrac{\partial T_\kappa}{\partial x} \right|_{x=0; \, x=x_{max}} = k_\kappa \left. \dfrac{\partial T_\kappa}{\partial y} \right|_{y=0; \, y=y_{max}} = h(T_f - T_\kappa)$ $k_m \left. \dfrac{\partial T_m}{\partial x} \right|_{x=0; \, x=x_{max}} = k_m \left. \dfrac{\partial T_m}{\partial y} \right|_{y=0; \, y=y_{max}} = h(T_f - T_m)$ $-k_m \left. \dfrac{\partial T_m}{\partial x} \right|_{x=x_{max}} = k_\kappa \left. \dfrac{\partial T_\kappa}{\partial y} \right|_{x=0} = q'' = U(T_m - T_\kappa)$

($s \equiv 1$ at 300 K 100% austenite, where s_0 is this predefined unity point).

$$Q_{\text{metal boss}} = \sum_i \int_0^{t_b} (\rho c)_{\text{Cu}} V_{\text{Cu},i} \cdot \dot{T}_{\text{Cu},i} \mathrm{d}t, \qquad (17)$$

$$Q_{\text{SMA}} = \sum_i \int_0^{t_b} (\rho c)_{\text{m}} V_{\text{m},i} \cdot \dot{T}_{\text{m},i} \mathrm{d}t, \qquad (18)$$

$$Q_{\text{air loss}} = \sum_i \int_0^{t_b} S_{\text{transfer},i} h(T_{\text{f}} - T_{\text{m},i}) \mathrm{d}t, \qquad (19)$$

$$s - s_0 = c_{p,\text{m}} \ln \frac{T_{\text{m}}}{T_0} - \Delta s \xi_{\text{M}}. \qquad (20)$$

For the sake of description, the upper surface midpoint of the metal boss is noted as point Q. The temperature at point Q drops rapidly from 35 °C to 27.7 °C in the first 5 s and then it takes 4.85 s to drop from 27.9 °C to the lowest temperature 26.2 °C at a slower rate. After 9.85 s, the SMA absorbs the heat from the environment together with the metal boss, causing both temperatures to rise, indicating the end of the discharge process.

The total stored cooling capacity of the SMA is 11204.1 J, of which 66% plays a fundamental role for cooling the metal boss by an average temperature drop of 8.8 °C, leaving 33% trapped in the SMA itself and 1% heat loss to the cabinet air. The effective volume-based energy storage density of the SMA is 11.97 J/g, and the energy storage efficiency and COP are 66% and 1.78, respectively.

5.2 Impact of initial condition

When setting the simulation parameters, the operating environment of the device is a constant 40 °C cabin. However, the temperature of the car cabin also varies non-uniformly and dynamically due to the uneven irradiation of the sunlight on the cabin and the continuous dynamic change of the sunlight intensity during the day, which may affect the cooling capacity of the car seat storage device. Figure 6 shows the results obtained by varying the initial temperature of the SMA and the metal boss before the discharging process, with all other conditions remaining constant.

The maximum temperature drop of the metal boss at 35 °C, 37 °C, and 40 °C varies little, only 0.3 °C, and the time it takes for the metal boss to reach the minimum temperature was not significantly different under the three conditions, which is within (10.0±0.2) s. As can be seen from Fig. 6 that the three curves are relatively stable, indicating that the cooling capacity of the device is relatively stable at different initial temperatures, with a

Table 2 Thermomechanical, model-specific, process-related parameters, and initial conditions used the simulations [22, 24–26]

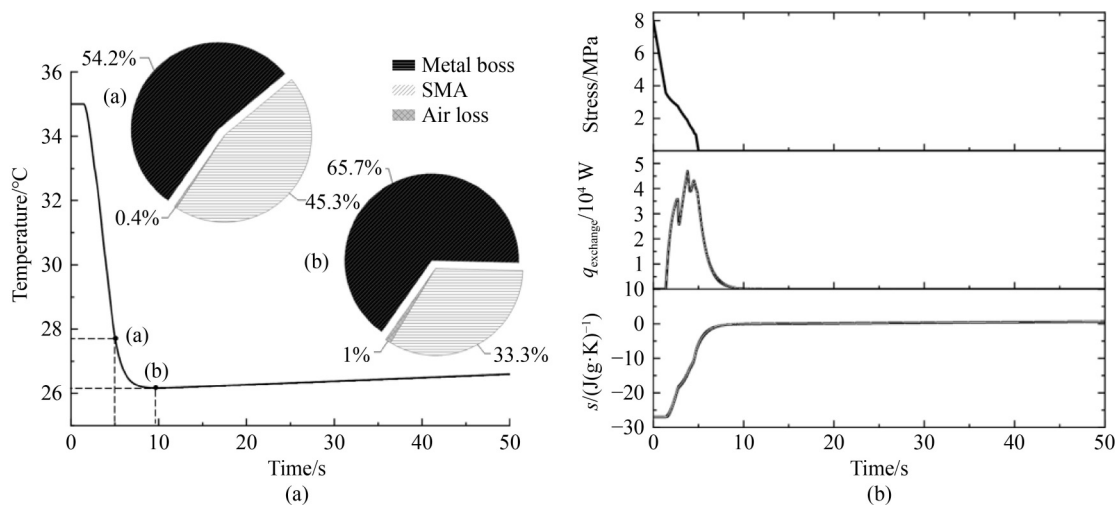| Symbol	Value	Symbol	Value
$C_{\text{AM}}/(\text{MPa·K}^{-1})$	10.4	$k_{\text{M}}/(\text{W·(m·K)}^{-1})$	8.6
$C_{\text{MA}}/(\text{MPa·K}^{-1})$	14.0	$k_{\text{Cu}}/(\text{W·(m·K)}^{-1})$	400
T_{As}/K	283.15	τ/s	1.0×10^{-3}
T_{Ms}/K	273.15	V_{L}/m^3	5×10^{-23}
ε_{T}	0.025	$h_{\text{f}}/(\text{W·(m}^2\text{·K)}^{-1})$	10
E_{A}/GPa	35.9	$U/(\text{W·(m}^2\text{·K)}^{-1})$	10000
E_{M}/GPa	32	$l_1 \times l_2 \times l_3/\text{mm}^3$	$350 \times 150 \times 3$
$\rho_{\text{m}}/(\text{kg·m}^{-3})$	6500	$\dot{\varepsilon}/\text{s}^{-1}$	0.01
$c_{p,\text{m}}/(\text{J·(kg·K)}^{-1})$	450	T_{f}/K	313.15
$\rho_{\text{Cu}}/(\text{kg·m}^{-3})$	8900	$T_{\text{m},0}/\text{K}$	308.15
$c_{p,\text{Cu}}/(\text{J·(kg·K)}^{-1})$	390	$T_{\text{Cu},0}/\text{K}$	308.15
$\Delta s/(\text{J·(kg·K)}^{-1})$	40	ε_{max}	0.05
$k_{\text{A}}/(\text{W·(m·K)}^{-1})$	18		

Fig. 5 Transient characteristics of discharging process.

(a) Temperature evolution of point Q and the breakdown of cooling capacity at timestamps (a) and (b); (b) transients of stress, specific entropy, and heat exchange rate.

maximum temperature drop ΔT_{max} of about 9 °C. However, although ΔT_{max} increases slightly at the high initial temperature, the cooling capacity of the car seat cold thermal energy storage device is limited. Therefore, the cooling result may not be in the acceptable comfort temperature range at higher initial temperatures.

5.3 Impact of geometric parameters

Aside from the planar SMA, there are also circular tubular and cylindrical SMAs. This paper also simulated the performance of the cold thermal energy storage device for three SMA geometric schemes (one cylindrical scheme named Case B, and two circular tubular schemes referred to as Case C and Case D). The total cross-sectional area of the above geometric solutions is controlled within $3 \times 10^{-4} - 4 \times 10^{-4} \mathrm{m}^2$, which makes the motor used in the baseline scenario applicable to all three cases.

For the cylindrical and tubular SMA, the second dimension is the number of tubes. The circular tube or cylinder is identical. They are arranged at equal intervals under the metal boss. In this case, cylindrical coordinate should be used for the energy equation of SMA, as expressed in Eq. (21).

$$(\rho c)_{\mathrm{m}} \frac{\partial T_{\mathrm{m},i}}{\partial t} = \frac{k(\xi)}{r^2} \frac{\partial}{\partial \varphi} \left(\frac{\partial T_{\mathrm{m},i}}{\partial \varphi} \right) + g'''. \qquad (21)$$

The simulated results for the other three schemes are sketched in Fig. 7. Of all schemes, Case A (original plate solution) has the lowest average temperature of 26.2 °C and the shortest time required to reach the lowest temperature of 9.85 s, while Case D has the highest average metal boss temperature of 29.4 °C and it takes the longest time to reach the minimum temperature of 53.52 s. The average minimum temperatures of the metal bosses in Cases B and C have a trivial difference at 28.2 °C and 28.0 °C. Obviously, as the contact area between SMA and the metal boss increases, the cooling rate

Fig. 6 Impact of initial temperature of discharging characteristic.

increases. Furthermore, the compact SMA geometry scheme effectively facilitates the improvement of the cold thermal energy storage efficiency because less cold remains in the SMA, and the reduced heat transfer area also leads less heat loss into the air. For instance, at the lowest temperature, Case B has the highest energy storage efficiency (66.8%), followed by Cases A (65.7%) and D (48.1%).

Although the thermal properties of the tubular SMA are inferior to those of cylindrical and plate SMAs, the mechanical properties of the tubular SMA are superior to those of the other two, which have a large moment of inertia and are slightly more resistant to buckling, decreasing the degree of deformation outside the horizontal direction during compression.

5.4 Different SMA materials

Ni-Ti SMAs have an excellent eCE, but nickel and titanium are expensive, while Cu-based SMAs are inexpensive and abundant. Compared with Ni-Ti SMAs, Cu-based SMAs usually have less transition strain and a lower critical transformation stress, although their eCE is inferior to Ni-Ti SMAs. At 4% strain, the maximum compressive stress of Ni-Ti alloy is 870 MPa, while that of CuAlZn is 450 MPa (nearly half that of Ni-Ti alloy) and that of CuAlMn is 130 MPa (about 1/7 that of Ni-Ti alloy) [27, 28].

Three SMA materials are selected for simulation comparison, which are $Ni_{50.4}Ti_{49.6}$, $Cu_{68}Al_{16}Zn_{16}$, and $Cu_{71.5}Al_{17.5}Mn_{11}$. Based on the properties of material, the maximum strain of $Cu_{71.5}Al_{17.5}Mn_{11}$ is set to 0.04. Figures 8(a) and (b) respectively show the temperature variation of the metal boss for a simulation time of 50 s under the constraint of fixed SMA geometry and motor power. The calculation results are summarized in Tables 3 and 4.

In the case of fixed SMA geometry, the cooling capacities of $Cu_{68}Al_{16}Zn_{16}$ and $Cu_{71.5}Al_{17.5}Mn_{11}$ are 4056.9 and 4535.6 J, respectively, about one-third of $Ni_{50.4}Ti_{49.6}$. In addition, the energy storage efficiency is not much different from the above cases, which is 62% and 63% for the former two and 66% for the latter. In the simulation of this section, the maximum stress and the compression power of $Cu_{68}Al_{16}Zn_{16}$ are 380 MPa and 6.1 W, respectively, while those of $Cu_{71.5}Al_{17.5}Mn_{11}$ are 160 MPa and 2.6 W, respectively, indicating that Cu-based SMAs may have a higher cold thermal energy storage capacity than Ni-Ti SMA due to the fact that more masses of Cu-based SMAs can be compressed to store cold thermal energy under the same loading power.

In the case of fixed motor power, the cooling capacity of $Cu_{68}Al_{16}Zn_{16}$ and $Cu_{71.5}Al_{17.5}Mn_{11}$ are 18865.7 and 43213.6 J, respectively. Although both are higher than that of $Ni_{50.4}Ti_{49.6}$ (11204.1 J), which is consistent with the analysis above, the thickness is increased to 12 and

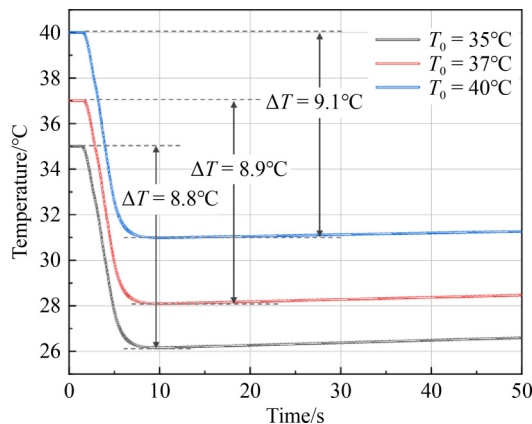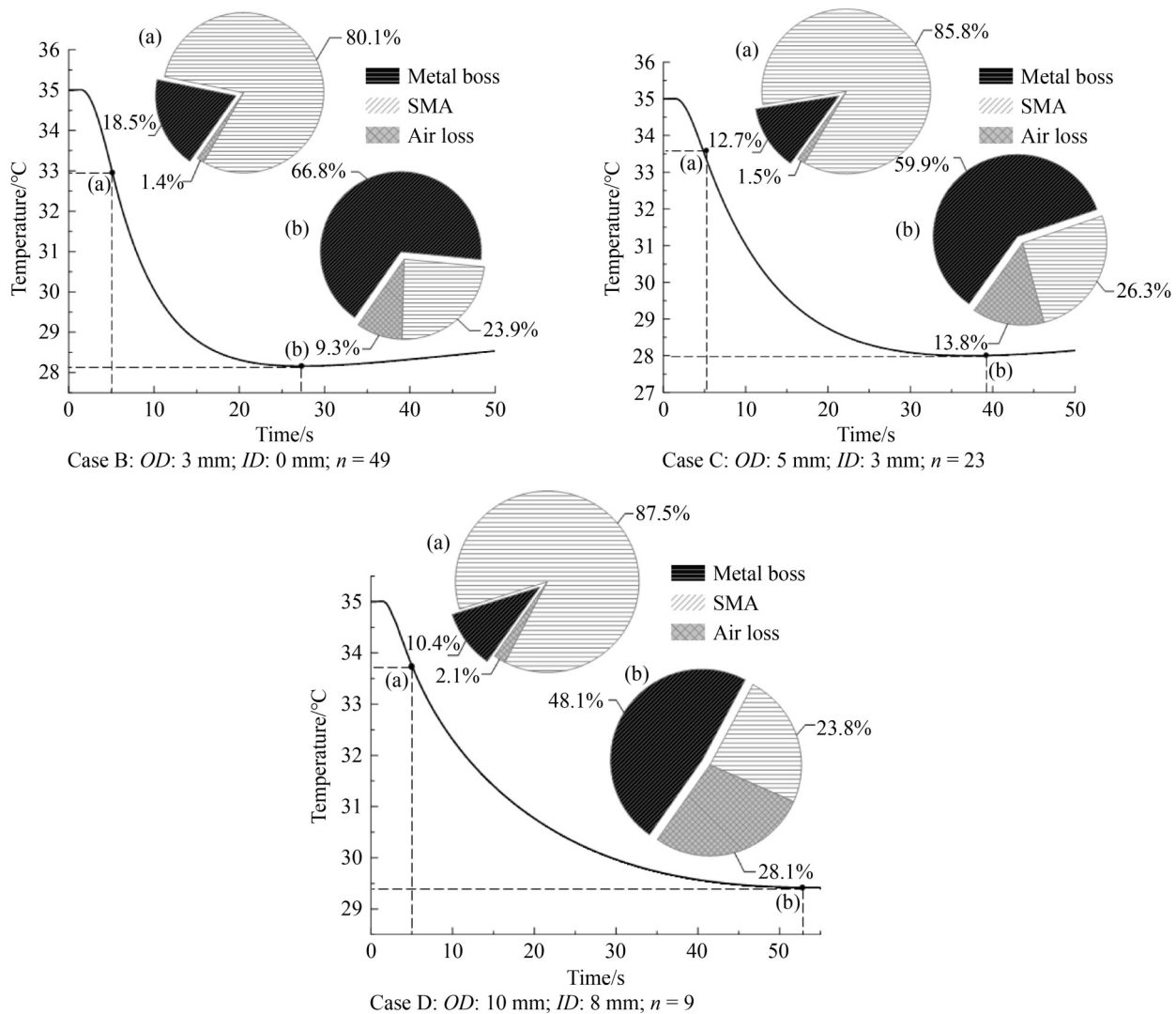**Fig. 7** Impact of different geometric schemes of SMA.

27 mm, and the volume is expanded by 4 and 9 times, respectively. The bulker Cu-based materials lead to a much lower energy storage efficiency than that of $Ni_{50.4}Ti_{49.6}$ because more cooling capacity generated by the SMA remains in the SMA at the moment when the average temperature of the metal boss reaches the minimum. In terms of thermal conductivity of the SMAs, Cu-based SMAs have a thermal conductivity of 5–10 times greater than that of Ni-Ti SMAs, which compensates for the possible delay in reaching the first co-temperature (the average minimum temperature that the metal boss can reach) due to the increase in volume.

Figure 8(c) shows the temperature change of the SMA during the unloading process, and the spot with the most significant temperature change on the upper or lower surfaces of the SMA is selected for visualization. It can be seen that the maximum temperature change of $Ni_{50.4}Ti_{49.6}$ is 17.8 °C, while those of $Cu_{68}Al_{16}Zn_{16}$ and $Cu_{71.5}Al_{17.5}Mn_{11}$ are 9.9 °C and 10.7 °C, respectively.

The driving force for temperature drop comes from the temperature difference between the metal boss and the SMA. When the initial temperature of the metal boss and the SMA is similar to each other, the temperature change of the SMA during the unloading process will limit the first co-temperature, which also limits the amount of cold thermal energy that the car seat receives, and eventually, leads to a lower energy storage efficiency. The cooling capacity distribution of the three elastocaloric materials at the minimum temperature of the metal boss at a fixed power is specifically illustrated in Fig. 8(d). Taking $Cu_{71.5}Al_{17.5}Mn_{11}$ for example, only 16.7% of the huge cooling capacity generated by the SMA is used on the metal boss, while 82.3% of that is left in itself, causing a low cooling utilization efficiency.

Even though Cu-based SMAs are inexpensive and readily available, all Cu-based SMAs must face the problem of the low fatigue performance associated with brittleness. Moreover, the latent heat of the two Cu-based
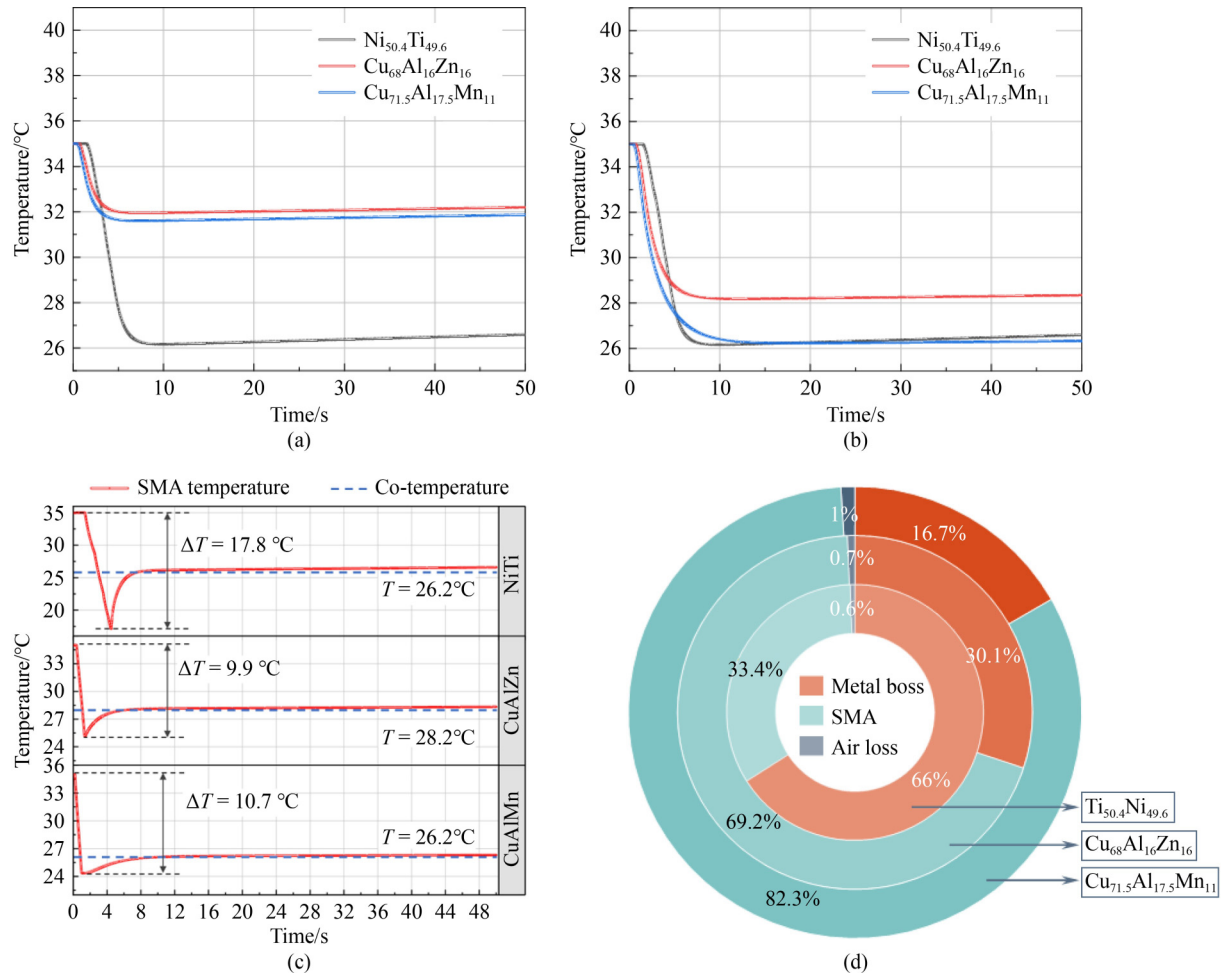
Fig. 8 Impact of elastocaloric materials.
(a) Temperature evolution of metal boss in fixed SMA geometry scheme; (b) temperature evolution of metal boss at fixed motor power;
(c) temperature change of three memory materials; (d) distribution of cooling capacity at the lowest temperature of metal boss.

Table 3 Results for the case of fixed SMA geometry

	$Ni_{50.4}Ti_{49.6}$	$Cu_{68}Al_{16}Zn_{16}$	$Cu_{71.5}Al_{17.5}Mn_{11}$
Q_{pro}/J	11204	4056.9	4535.6
η/%	66	62	63
$T_{Cu,min}$/°C	26.2	31.7	32.0
W/W	23.0	6.1	2.6
ε_{max}	0.05	0.05	0.04
σ_{max}/MPa	800	380	160

Table 4 Results for the case of fixed motor power

	$Ni_{50.4}Ti_{49.6}$	$Cu_{68}Al_{16}Zn_{16}$	$Cu_{71.5}Al_{17.5}Mn_{11}$
Q_{pro}/J	11204	18865.7	43213.6
η/%	66	30	17
$T_{Cu,min}$/°C	26.2	28.2	26.2
W/W	23.0	24.4	23.4
COP	1.78	1.30	1.71

SMAs used in the simulation is less than 50% of that of the existing Ni-Ti SMAs, which limits their practical applications.

6 Conclusions

This paper presents the principle of using SMAs for cold thermal energy storage applications. SMAs are not only solid-state refrigerants but also good candidates for thermal energy storage materials. The design of a car seat cold thermal energy storage device is presented based on the proposed theoretical SMA cold thermal energy storage cycle. The device leverages the shape characteristics of the inclined slide track to load or unload the SMA, and the motor is controlled by a pressure sensor to drive the cable to pull the SMA up and down. Besides, transient variations of temperature, stress, specific entropy, and discharging rate are presented. The simulation results indicate that the minimum temperature

of the metal boss under the seat reaches 26.2 °C at 9.85 s after the discharging process initiates, which demonstrates a temperature reduction of 8.8 °C in the car seat. In addition, the energy storage efficiency of the device is 66%; the time-averaged compression power for a 5-min loading process is 20.4 W, corresponding to the COP of 1.78. Furthermore, this paper discusses the effects of initial temperature, elastocaloric material, and geometry scheme of SMAs on the performance of the car seat cold thermal energy storage device. It can be concluded that

1) The cooling capacity of the cold thermal energy storage device for car seat based on SMA is relatively stable with a temperature drop of about 9 °C.

2) A positive correlation exists between the cooling rate and the contact area between the SMA and the metal boss under the seat, and the compact SMA geometry facilitates more efficient cooling of the device.

3) Although Cu-based SMAs are cheaper and have a smaller phase transition stress, which contributes to a large cooling capacity of the device at the same compression power, they have a lower latent heat value and a smaller SMA temperature drop, which limits the amount of cooling that is extracted by the metal boss. Thus, the performance of Cu-based SMAs is generally worse than that of Ni-Ti SMA.

Increasing the thermal conductivity of SMAs can facilitate the discharging process, while reducing phase change stress and increasing latent heat value can effectively improve the energy storage efficiency. It is hoped that this work is a starting point to attract more ambitious multidisciplinary researchers with different backgrounds to work together on the new concept that is proposed in this study.

Competing interests The authors declare that they have no competing interests.

Notations

a	Thermal diffusivity/(m²·s⁻¹)
COP	Coefficient of performance
C	Clausius-Clapeyron coefficient/(MPa·K)
c_p	Specific heat/(J·(kg·K)⁻¹)
eCE	Elastocaloric effect
E	Young's modulus/MPa
g'''	Generation term in energy equation/(W·m⁻³)
h	Heat transfer coefficient/(W·(m²·K)⁻¹)
k	Thermal conductivity/(W·(m·K)⁻¹)

l	Length/m
Q	Heat transfer/J
S	Surface area/m²
Δs	Entropy change/(J·(kg·K)⁻¹)
SMA	Shape-memory alloy
s	Specific entropy/(J·(kg·K)⁻¹)
T	Temperature/K
U	Solid-solid heat transfer coefficient/(W·(m²·K)⁻¹)
V	Volume/m³
V_L	Transforming layer volume/m³

Greek symbols

ε	Strain
$\dot{\varepsilon}$	Strain rate/s⁻¹
η	Energy storage efficiency
ξ	Phase fraction
ρ	Density/(kg·m⁻³)
τ	Relaxation time constant/s
σ	Stress/MPa

Subscripts

A	Austenite
As	Austenite start
Af	Austenite finish
Cu	Copper
c	Cooling capacity in one cycle
f	Air
M	Martensite
Ms	Martensite start
Mf	Martensite finish
max	Maximum
m	SMA

Superscripts

AM	Austenite to martensite transformation
MA	Martensite to austenite transformation

References

1. Da Cunha J P, Eames P. Thermal energy storage for low and medium temperature applications using phase change materials—a review. Applied Energy, 2016, 177: 227–238

2. Qian X. Pumping into a cool future: electrocaloric materials for zero-carbon refrigeration. Frontiers in Energy, 2022, 16(1): 19–22

3. Nazir H, Batool M, Osorio F J B, et al. Recent developments in phase change materials for energy storage applications: a review. International Journal of Heat and Mass Transfer, 2019, 129: 491–523

4. Mediwaththe C P, Shaw M, Halgamuge S, et al. An incentive-compatible energy trading framework for neighborhood area networks with shared energy storage. IEEE Transactions on Sustainable Energy, 2020, 11(1): 467–476

5. Lencer D, Salinga M, Wuttig M. Design rules for phase-change materials in data storage applications. Advanced Materials, 2011, 23(18): 2030–2058

6. Quarini J, Prince A. Solid state refrigeration: cooling and refrigeration using crystalline phase changes in metal alloys. Proceedings of the Institution of Mechanical Engineers. Part C, Journal of Mechanical Engineering Science, 2004, 218(10): 1175–1179

7. Fallahi A, Guldentops G, Tao M, et al. Review on solid-solid phase change materials for thermal energy storage: molecular structure and thermal properties. Applied Thermal Engineering, 2017, 127: 1427–1441

8. Sharar D J, Donovan B F, Warzoha R J, et al. Solid-state thermal energy storage using reversible martensitic transformations. Applied Physics Letters, 2019, 114(14): 143902

9. Cong D, Xiong W, Planes A, et al. Colossal elastocaloric effect in ferroelastic Ni-Mn-Ti alloys. Physical Review Letters, 2019, 122(25): 255703

10. Brinson L C. One-dimensional constitutive behavior of shape memory alloys: thermomechanical derivation with non-constant material functions and redefined martensite internal variable. Journal of Intelligent Material Systems and Structures, 1993, 4(2): 229–242

11. Chen Y, Wang Y, Sun W, et al. A compact elastocaloric refrigerator. The Innovation, 2022, 3(2): 100205

12. Hite N, Sharar D J, Trehern W, et al. NiTiHf shape memory alloys as phase change thermal storage materials. Acta Materialia, 2021, 218: 117175

13. Sharar D J, Leff A C, Wilson A A, et al. High-capacity high-power thermal energy storage using solid-solid martensitic transformations. Applied Thermal Engineering, 2021, 187: 116490

14. Chluba C, Ge W, Lima de Miranda R, et al. Shape memory alloys. Ultralow-fatigue shape memory alloy films. Science, 2015, 348(6238): 1004–1007

15. Ossmer H, Chluba C, Gueltig M, et al. Local evolution of the elastocaloric effect in TiNi-based films. Shape Memory and Superelasticity, 2015, 1(2): 142–152

16. Li S, Cong D, Sun X, et al. Wide-temperature-range perfect superelasticity and giant elastocaloric effect in a high entropy alloy. Materials Research Letters, 2019, 7(12): 482–489

17. Emaikwu N, Catalini D, Muehlbauer J, et al. Experimental investigation of a staggered-tube active elastocaloric regenerator. International Journal of Refrigeration, 2022, online, https://doi.org/10.1016/j.ijrefrig.2022.09.006

18. Qian S, Geng Y, Wang Y, et al. Design of a hydraulically driven compressive elastocaloric cooling system. Science and Technology for the Built Environment, 2016, 22(5): 500–506

19. Tušek J, Engelbrecht K, Eriksen D, et al. A regenerative elastocaloric heat pump. Nature Energy, 2016, 1(10): 1–6

20. Tušek J, Engelbrecht K, Mikkelsen L P, et al. Elastocaloric effect of Ni-Ti wire for application in a cooling device. Journal of Applied Physics, 2015, 117(12): 124901

21. Qian S, Geng Y, Wang Y, et al. A review of elastocaloric cooling: materials, cycles and system integrations. International Journal of Refrigeration, 2016, 64: 1–19

22. Qian S, Yuan L, Yu J, et al. Numerical modeling of an active elastocaloric regenerator refrigerator with phase transformation kinetics and the matching principle for materials selection. Energy, 2017, 141: 744–756

23. Tušek J, Engelbrecht K, Millán-Solsona R, et al. The elastocaloric effect: a way to cool efficiently. Advanced Energy Materials, 2015, 5(13): 1500361

24. Wendler F, Ossmer H, Chluba C, et al. Mesoscale simulation of elastocaloric cooling in SMA films. Acta Materialia, 2017, 136: 105–117

25. Qian S, Alabdulkarem A, Ling J, et al. Performance enhancement of a compressive thermoelastic cooling system using multi-objective optimization and novel designs. International Journal of Refrigeration, 2015, 57: 62–76

26. Chen J, Zhang K, Kan Q, et al. Ultra-high fatigue life of NiTi cylinders for compression-based elastocaloric cooling. Applied Physics Letters, 2019, 115(9): 093902

27. Bonnot E, Romero R, Mañosa L, et al. Elastocaloric effect associated with the martensitic transition in shape-memory alloys. Physical Review Letters, 2008, 100(12): 125901

28. Qian S, Geng Y, Wang Y, et al. Elastocaloric effect in CuAlZn and CuAlMn shape memory alloys under compression. Philosophical Transactions. Series A. Mathematical, Physical and Engineering Science, 2016, 374(2074): 20150309